Morphological and Mechanical Characterization of Thrombi in Abdominal Aortic Aneurysms

Leonet Joris, Valerie Deplano

Morphological and Mechanical Characterization of Thrombi in Abdominal Aortic Aneurysms

Joris Léonet[a], Jérôme Vicente[b] and Valérie Deplano[a,*]

[a]Aix-Marseille Univ, CNRS, Ecole Centrale Marseille, IRPHE, Marseille, 13013, France

[b]Aix-Marseille Univ, CNRS, IUSTI, Marseille, 13013, France

ARTICLE INFO

Keywords:

Human thrombi

AAA

Imaging

Mechanical tests

Models

ABSTRACT

Thrombi are found in most abdominal aortic aneurysms, influencing the intrinsic properties of the vessel wall and potentially contributing to rupture. This review summarizes studies conducted to characterize the morphological and mechanical properties of thrombi from abdominal aortic aneurysms at both macroscopic and microscopic scales. A variety of *in-vivo* and *ex-vivo* approaches including imaging and mechanical experiments have been employed, and the results demonstrate: (1) the importance of the porous aspect in the cell filtration and vessel wall weakening, (2) hyperelasticity and viscoelasticity used to describe thrombi behavior, and (3) a lack of aggregated experimental data. Further research is required to develop multi-axial mechanical approaches for a more comprehensive characterization of the ILT, as well as to incorporate ILT remodeling into constitutive models.

1. Introduction

Cardiovascular diseases attributed to factors like hypertension, diabetes, obesity or smoking, are the primary cause of death worldwide with about 17.9 million deaths each year (1). Some of these pathologies directly affect the aorta such as aortic aneurysms or dissections. Aortic aneurysms are abnormal, localized dilations of the aorta, defined as an enlargement exceeding 1.5 times the original diameter of a specific aortic segment, most commonly occurring in the abdominal or thoracic regions. An aortic dissection results in a tear in the aortic wall creating a false lumen of blood circulation. This dissection can occurs in the ascending or descending thoracic aorta. Aortic aneurysm rupture and aortic dissection represent significant global public health challenges, impacting hundreds of thousands of individuals annually (2; 3; 4; 5). The mortality rate is alarmingly high, reaching 90% for ruptured abdominal aortic aneurysms (6) and 50% within the first 48 hours of symptom onset for aortic dissection (7).

In the majority of cases, the aneurysmal region and the false lumen are preferential sites of thrombus formation. The thrombus is a highly complex and heterogeneous structure made of cellular elements such as red blood cells (RBC), white blood cells (WBC) and platelets (PLT), nested in a fibrin network. Actually, several questions are not fully resolved, including the complex on multi-factorial mechanisms of thrombus evolution and role in the progression of the pathology.

Over the past 30 years, the study of aortic thrombi brought a multidisciplinary approach involving clinicians, biologists and biomechanics, with the aim of giving answer to: (i) How to monitor aortic thrombus formation and evaluate its age ? (ii) Does thrombus have a detrimental role in the evolution of aortic pathologies ? (iii) How to build a representative model ?

Actually, studies investigated morphological, mechanical and fluid properties of aortic thrombi to better understand its physiological behavior. Various imaging techniques were employed to capture the thrombus morphology, ranging

*Corresponding author

valerie.deplano@univ-amu.fr (V. Deplano)

ORCID(s): 0009-0005-6443-0055 (J. Léonet)

from macroscopic imaging with magnetic resonance imaging (MRI) to microscopic analysis using histology, scanning electron microscopy (SEM), and X-ray micro-computed tomography (micro-CT), each offering unique advantages and limitations. The mechanical characteristics were determined using various approaches including compression, tensile and shear experiments to understand thrombus behavior and define constitutive models. However, as no standard mechanical testing protocol exists and as the results of the different approaches were not aggregated, it is complicated to link most of the mechanical results. Finally, most of the experiments studied the aortic thrombus at macroscopic scale and only few provided microscopic quantitative data.

Currently, collecting human thrombus samples is highly challenging. Some studies observed human thrombi from aortic dissections at macroscopic scale, but only a limited number have explored them at microscopic scale, primarily using murine models (8; 9; 10). Regarding thoracic aortic aneurysms (TAA), only macroscopic investigations were performed and no research has focused on examining the microstructure of human thrombi from the descending region. The available information is limited to recent case reports that describe fully removed thrombi (11) but lack detailed microstructural and mechanical characterization. Lastly, very few studies investigated the microstructure of human thrombi in the ascending region using histological techniques (12; 13; 14). Macroscopic qualitative results of thrombi from TAA or aortic dissections alone are insufficient to accurately characterize the thrombi. Based on these findings, we decided to focus our review on both morphological and mechanical characterization of the human thrombus from abdominal aortic aneurysms (HT-AAA) only. For several years, efforts were indeed made to conduct experimental studies on HT-AAA. A commonly suggested hypothesis addresses the detrimental role of the thrombus in the progression of the pathology (15). This hypothesis emerged from a combination of macroscopic and microscopic imaging analyses coupled with mechanical investigations, leading to constitutive models.

Using Google Scholar, all relevant publications describing experimental characterization of the HT-AAA were reviewed. A total of thirty studies were selected following the review process. For MRI and histology, a specific criterion was applied to include only quantitative studies. For the remaining studies, no selection criteria were applied, and all studies were included. To resume, this review explores current experimental methods for characterizing thrombus morphology and mechanical properties, offering a critical lighting of their contributions to understanding the thrombus's role in AAA progression, evaluate its age, develop constitutive models, and suggesting future research directions.

2. General description of thrombi

A simplified macroscopic description of thrombus formation can be explained by the disruption of the mechanisms of hemostasis, the process that maintains normal blood circulation after vascular damage. The hemostasis is a natural process that can be separated into three phases; platelets recruitment to the site of injury, blood coagulation leading to thrombin and fibrin formation, and then fibrinolysis that leads to the dissolution of thrombus. The resulted thrombus is a fibrous, porous and inhomogeneous structure. But sometimes, regulatory mechanisms of hemostasis are compromised by pathological processes and overproduction of thrombin occurs, leading to thrombosis (16). There are two main types of thrombosis: arterial and venous. These pathological thrombi can clog a vessel at their site of formation or create a blockage in another location (usually smaller vessels) when a piece of thrombus detaches (emboli).

When focusing on aortic thrombi called intraluminal thrombus (ILT), it has been found special due to its different formation mechanism and the fact that no vessel clogging occurs. In the case of aortic aneurysms, the geometry of the aorta is modified by an enlargement modifying blood flow behavior. The modified hemodynamics in these geometric singularities can partly explain ILT formation and evolution (17). Related mechanisms are described in Figure 1. First, non-activated platelets (orange in Figure 1) are trapped inside vortical structures formed at the AAA entrance (18). Then, vortical structures propagate downstream while activating platelets due to higher shear stress (18). At this step, there is a mixing between non and activated platelets (yellow in Figure 1). Finally, activated platelets are released after the collapse of vortical structures and adhere to sites of low wall shear stress (WSS) (18). With aggregation and time, an inhomogeneous, multilayered, porous structure with permeability gradients is formed called ILT (Figure 1). The three layers are respectively called luminal, medial and abluminal from the lumen to the wall (Figure 1).

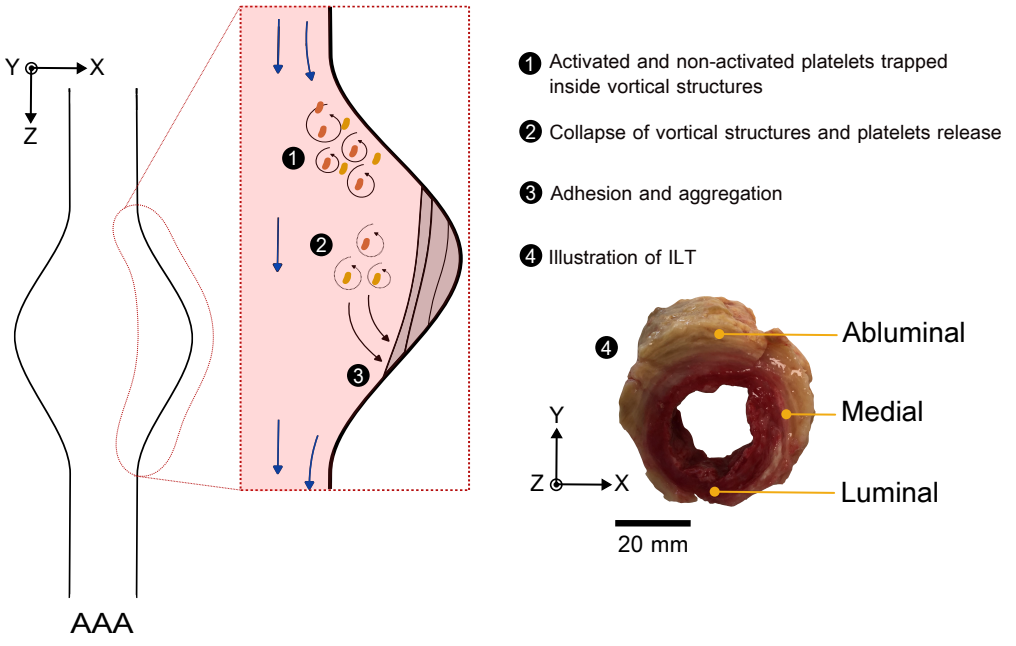

Figure 1: Formation process of ILT in AAA.

3. ILT morphology and composition

Imaging methods aim to characterize the complex morphological features of thrombi. Understanding the intricate structures of thrombi is crucial for gaining insights into their formation, stability, mechanical behavior and potential clinical implications. Each of the reviewed imaging methods provides more or less quantitative answers to different questions related to ILT. We have proposed a quantitative list of the most common and new *in-vivo*/*ex-vivo* imaging approaches for obtaining the microstructure and composition of ILT.

3.1. MRI

Several factors, such as ILT size and its internal heterogeneous structure, were linked to AAA growth and rupture (19; 20). While studies using computed-tomography (CT) or MRI demonstrated that ILT size influences AAA growth, the role of its complex internal structure remains poorly understood (19). Compared to CT or ultrasounds (US), MRI allowed to reach better image contrast leading to an accurate ILT internal structure *in-vivo* visualization (19). Quantitative MRI studies on ILT were reviewed and are presented in supplementary material 1.

A study investigated the efficiency of visualizing ILT internal structure using MRI making the distinction between organized and non-organized structures (19). This organization depends on the ILT age and its level of delamination with higher non-organized structures for old thrombi (19). Complementary insights were provided linking ILT macroscopic aspects with quantitative MRI signal intensity ratio (SIR) (20). The ILT was classified in three categories: (1) solid homogeneous appearance (SIR=1.25 $\pm$ 0.22), (2) thin luminal layer and mainly delaminated structure considered as fresh (SIR=2.08 $\pm$ 0.20), and (3) multilayered heterogeneous structure (SIR=1.83 $\pm$ 0.42) (20). SIR were significantly different between categories (1) and (2) (20). Moreover, high SIR were associated with delaminated structures. However, as category (3) was a combination between categories (1) and (2) in terms of structures, no significant SIR difference was found (20). The image quality highly depends on the MRI sequence type and protocol. More recent studies tried to better visualize internal ILT structure using different MRI approaches. A study conducted non-contrast black blood MRI technique on ILT in order to reach better spatial resolution (around 0.75×0.75×2 mm) and contrast (21). As the black blood technique suppressed the blood signal, better visualization of surrounding tissues as ILT was possible. This method was better for characterizing fresh ILT compared to conventional MRI (21). Another study correlated a link between ILT category and AAA growth rate using MRI (22). They demonstrated that category (2), corresponding to fresh ILT, led to higher AAA growth rate with 3.03 cm^2/year against 1.6 cm^2/year for category (1)

with homogeneous solid ILT (22). A potential explanation is that more solid ILT are better in reducing wall stress. Just like the internal structure, the biological active aspect of the ILT may be associated with AAA evolution. Using *in-vivo* and *ex-vivo* superparamagnetic iron oxide (SPIO) MRI, some works showed that the WBC infiltrated the luminal region of the ILT based on the amount of SPIO particles, compared to abluminal region. The high amount of WBC may potentially indicate protease release in the ILT, as elevated proteolytic activity levels are known to contribute to rupture (23). These findings could help in better evaluate clinical risks (23).

To conclude, actual MRI findings correlate ILT size with AAA growth principally (19; 20; 22), specifying that unorganized loose ILT lead to higher AAA growth rate based on high MRI signal intensities (22). Moreover, MRI is the only *in vivo* technique capable of distinguishing the different structural organizations of ILT, unlike the commonly used CT. However, this method is limited by the low contrast and spatial resolution (1×1×2 mm) of the images making it difficult to visualize thrombus structure in detail. New approaches as black blood technique were developed to improve the image quality (21) but these protocols are difficult to implement in routine clinical practice (costly and time-consuming). Recognizing these limitations, alternative techniques may offer a more in-depth exploration of ILT microstructure and composition, particularly when based on *ex-vivo* human samples.

3.2. Histology

Histological examination plays a crucial role in visualizing the details of thrombus morphology and composition, providing insights complementary to non-invasive imaging techniques such MRI. Continuing to be regarded as the gold standard, this methodology probes the microscopic domain, revealing the intricate cellular and molecular details influencing the development, stability, and potential clinical implications. Quantitative histological data on ILT microstructure are still lacking, as it is difficult to obtain human samples since the advent of endovascular surgery. We decided to review quantitative histological analyses of ILT, as detailed in supplementary material 2, to determine whether specific ILT components (cells, proteins, etc.) and structural features contribute to the weakening of the aortic wall.

Histological investigations were conducted and demonstrated networks of interconnected canaliculi within ILT, with an area that increases with distance from the luminal (24). With their size comprised between 5 to 36 μm^2, the porous networks may allow the macromolecules and cells passage but only in regions near the lumen (24). Another work highlighted a limited cellular penetration to the medial layer (25). As this porous aspect might plays a role in the aortic wall feeding and AAA growth, a study provided quantitative porosity data on ILT resulting in a mean value of $\approx 20\%$ for all three layers (26). Then, new insights linking both ILT thickness and microstructure with age, classifying four different phases: (1) presence of RBC only with a loose fibrin network, (2) loose fibrin network with less cells, (3) condensed fibrin network with thick bundles, and (4) condensed fibrin network without pores and no cells, with RBC concentration that decreased with age (from 80% to 0%) (27). The ILT composition also revealed a high amount of inflammatory cells (between 1.5% to 3% of WBC) and the presence of other specific proteins such as oxygen-regulated protein (ORP) (28) or matrix metalloproteinases (MMP) (28) using immunohistochemistry, justifying the AAA wall weakening by hypoxia and excessive proteolytic activity (27; 28). These findings were also observed qualitatively in other studies (29; 25). In fact, MMP-9 are associated with the development of neutrophil proteases that can degrade all matrix fibrillar proteins and thus provoke wall rupture. Moreover, the absence of RBC in the outer ILT region could contribute to wall hypoxia (24; 27; 29). Finally, histology may be useful to investigate potential issues linked with new AAA treatments approaches such as endovascular aneurysm sealing system (EVAS). A study revealed a fluid-displacement from ILT when applying pressure (30). As a result, a decrease of thrombus volume during and after EVAS procedure, that may potentially impaired the stability of the endobags and position of the stent frames in the abdominal aorta (30).

These findings provided deeper insights into the formation and function of ILT. Thrombus is a highly heterogeneous

porous structure composed of fibrin fibers, with cells predominantly located in the luminal layer. The entrapment of cells, particularly RBCs, in the luminal region, combined with the presence of proteins that serve as markers of hypoxia, suggests that the ILT significantly influences the integrity of the aortic wall and can provoke rupture. However, it is crucial to acknowledge the limitations inherent in obtaining quantitative data on ILT microstructure such as the low resolution of light microscopy (typically between 0.35 to 0.5 μm). The only quantitative porosity values were obtained after eliminating pores smaller than 14 µm diameter (26), making results unreliable. Moreover, histological sample preparation, including fixation, embedding, sectioning, and staining, introduces alterations to the microstructure, particularly during fixation and sectioning, potentially leading to unreliable morphological data (26). Furthermore, the studies predominantly relied on qualitative and/or quantitative assessments based on 2D sections, emphasizing the need for 3D information to better delineate how cells navigate within distinct thrombus layers.

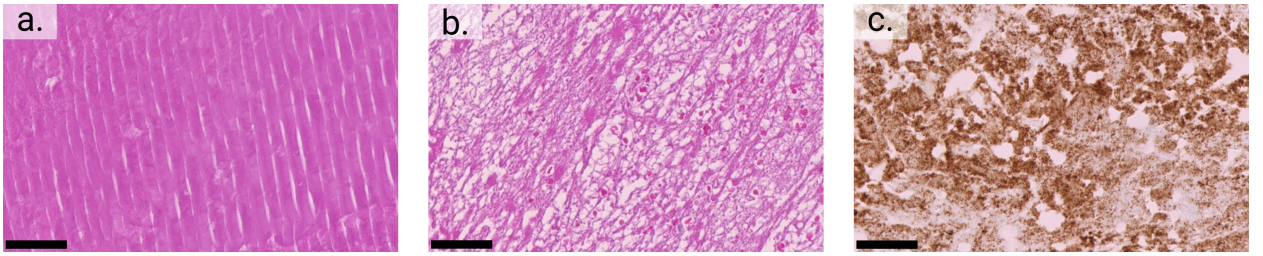

Figure 2: Histological sections of an ILT removed from an AAA. (a) Abluminal region stained with HE showing oriented and condensed fibrin fibers with no porosity. (b) Medial region stained with HE showing fibrin fibers with thick bundles with sometimes packs of agglomerated RBCs in pores. (c) Luminal region stained with CD61 showing a high amount of platelets (brown) with loose fibrin fibers. The scale bars are equal to 50 μm (adapted from (29)) [**Note: I am an author of this article; Copyright: CC BY-NC-ND 4.0**, permission pending from Taylor & Francis**].

3.3. SEM

In order to reach higher 2D image resolution (tens of nanometers) and magnification, SEM may be used to visualize in detail tissue structures and components with a significant depth of view. All SEM studies on ILT presented in supplementary material 3. A study observed the ILT using SEM and confirmed the histological hypothesis of an existing continuous interconnected network of canaliculi, starting branching at the luminal region (24). The cellular presence in the luminal layer was also confirmed by observing platelets, RBC and macrophages. The overall findings suggested that all cells were trapped when penetrating into this network of canaliculi, contributing to the aortic wall weakening. Another study observed the three ILT layers structure and justified notable differences with a luminal made of identifiable fibrin fibers with varying degrees of fineness, and compared to the two other layers with degenerated fibers that increases the further away from luminal (31). These observations were also confirmed by an other work (32) that presented a heterogeneous porous structure in relation the the formation process in successive layers. As demonstrated in the majority of studies (24; 27; 29; 25), the ILT structure varied greatly within the same ILT, but also between different patients which can have a different impact on the pathology. The importance of the structural heterogeneity was highlighted and demonstrated that ILT may be mainly made of large dense fibrin-rich regions influencing cell transport (33). Consequently, the ILT degradation might be reduced because of low fibrinolysis stabilizing the ILT size (33). Paired with SEM, energy dispersive X-ray spectroscopy (EDX) allows the determination of elemental composition. Using this approach, a study performed SEM and EDX analysis on both AAA wall and different ILT types based on their macroscopic appearance (Figure 3), and observed calcifications within the wall when associated with ILT that may reduce the vessel wall integrity and lead to potential rupture (34).

SEM is a valuable tool for acquiring detailed structural and compositional information about ILT. The same findings

as histology were observed with an ILT structure made of interconnected network of canaliculi, where cells are only present in the luminal region. The presence of calcifications paired with the lack of cells in the outer wall region suggest that the ILT may provoke wall rupture. However, obtaining representative quantitative data can be labor-intensive, as the imaged areas are typically small (a few microns). Furthermore, quantitative and relative surface findings were derived from prepared thrombi, involving processes such as fixation, dehydration, coating, and sometimes drying, which can alter the morphology similarly to histological methods. Addressing these challenges necessitates the adoption of new methods that can provide reliable 3D morphological data.

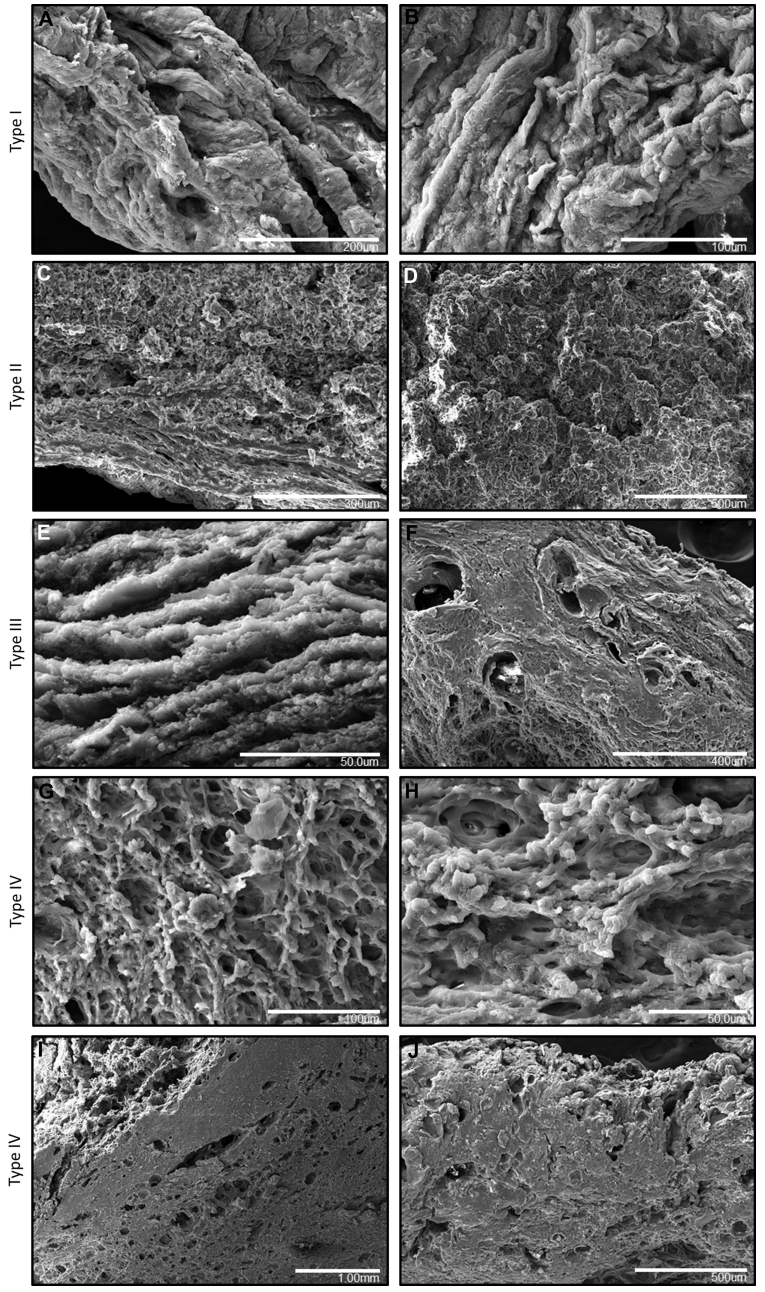

Figure 3: SEM images of different ILT types. (A,B,C,E,G) luminal layer. (D,F,H) medial layer. (I) transition between medial and abluminal layer and (J) abluminal layer (taken from (34) with permission).

3.4. X-ray micro-computed tomography

Micro-CT is a high-resolution 3D imaging technique (up to 0.5 μm resolution) that allows the visualization of both internal and external morphologies of biological samples using X-rays. Compared to conventional imaging methods (histology, SEM, etc.), micro-CT is non-destructive with scanning time that can vary from seconds to hours (35). However, due to the low contrast when imaging soft biological tissues, contrast agents may be used to binds specific components, known as contrast-enhanced micro-CT (CE-MCT) (35). Given the highly complex 3D morphology of ILT, this approach could provide valuable insights into the mechanisms of cell navigation within its structure, which are not yet fully understood. We decided to propose an exhaustive list of micro-CT studies on ILT as presented in supplementary material 4.

As demonstrated in the majority of works (24; 25; 28; 36), the cell filtration within the ILT may play a crucial role in the aortic wall weakening explanation. In fact, depending on the architecture, the cells may or may not penetrate the ILT (24; 25). Based on precedent works on myocardial thrombi (37; 38), a study observed the 3D microstructure of ILT using CE-MCT at 3 μm resolution (29) (Figure 4). First results showed comparative structures with previous histological investigations (27), that means a luminal made of loose fibrin fibers, a medial with more condensed fiber creating larger pores and finally a dense abluminal region. Compared to previous findings (26), different and lower porosities were reported for all three layers with comparable values for both luminal and medial regions of 8% while 4% was reported for the abluminal (29). Moreover, smaller pores were observed in the luminal layer with mean values of 9 μm compared to 29 μm for the two others. These results seem surprising, since previous results showed that the areas with the largest pores are devoid of cells (24; 27). But these observations highlighted the importance of pore interconnection, also mentioned by a previous study (24). Based on micro-CT images, interconnected networks were observed over the entire luminal region only leading a permeability value around $10^{-14} m^2$. This results may justified the presence of cells in the luminal region. As classical used CE-MCT alters the morphological ILT properties (39) with an experimental protocol similar to histology and SEM, a new protocol that maintains the physiological ILT properties was developed (40). The results showed a higher porosity with a similar value for both luminal and medial layers around 13%, while 4% was reported for the abluminal layer (40). Finally, a fluid-permeable luminal region was observed with values between $1.7 \times 10^{-15} m^2$ and $1.9 \times 10^{-14} m^2$ (40).

Micro-CT findings highlighted the importance of pore interconnection in the cell filtration within ILT structure. These results confirm once again the role of ILT in the vessel wall weakening. However, some limitations are associated with the use of micro-CT technique. First, the access to such facility is often limited and setting up a reliable protocol is labor-intensive and time-consuming. When using commonly used preparation protocol for biological tissues, both morphological and mechanical properties are altered (39; 41) and new protocol need to be used (40). As the different components within the structure cannot be identified in a single sample where only grayscale variations are observed, these variations likely correspond to different ILT components. High grayscale regions, for instance, may indicate RBC-rich areas (42). Finally, a critical need remains for additional quantitative data to enhance the characterization of ILT microstructure and establish connections with mechanical properties.

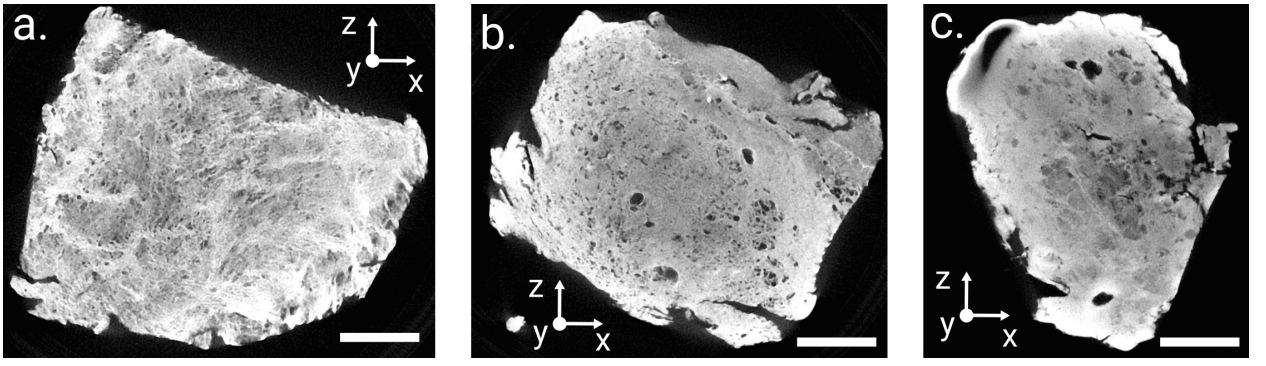

Figure 4: CE-MCT images of ILT samples using PTA staining showing the heterogeneity of the different ILT layers. (a) Luminal layer. (b) Medial layer. (c) Abluminal layer. The scale bars are equal to 0.5 mm (adapted from (29)) [**Note: I am an author of this article; Copyright: CC BY-NC-ND 4.0**, permission pending from Taylor & Francis**].

4. ILT mechanical characterization

Mechanical tests are essential to understand tissue response characteristics and provide crucial insights for building models. Some studies were conducted on *in-vivo* thrombi to assess tissue stiffness and ascertain their ages. Techniques such as strain elastography, as demonstrated in the work of (43), and shear-wave elastography, as evidenced in the study of (44), were employed for this purpose. However, these techniques have several limitations. In fact, a high amount of studies were conducted on animal models (45) and the majority concerned deep-vein thrombus (44; 45). Moreover, obtaining accurate quantitative data using elastography can be challenging due to the spatial resolution (on the order of millimeters), and the qualitative interpretation of the obtained results is notably operator-dependent, as mentioned in multiple studies (43; 44). For these reasons, we decided to focus on human ILT *ex-vivo* mechanical experiments only (supplementary material 5). Key experimental parameters must be emphasized as they significantly influence mechanical results: (i) sample preparation, dimensions and geometry (illustrated in Figure 5 for clarity), (ii) testing systems (gripping mechanisms, load cell, etc.), (iii) stress and deformation parameters (preconditioning, physiological deformation range, loading rate, etc.), (iv) tissue hydration conditions (e.g., thermostatic bath, native environment, or saline solution), and (v) metrology for displacement measurements (ceramic markers, speckle, digital image correlation, etc.).

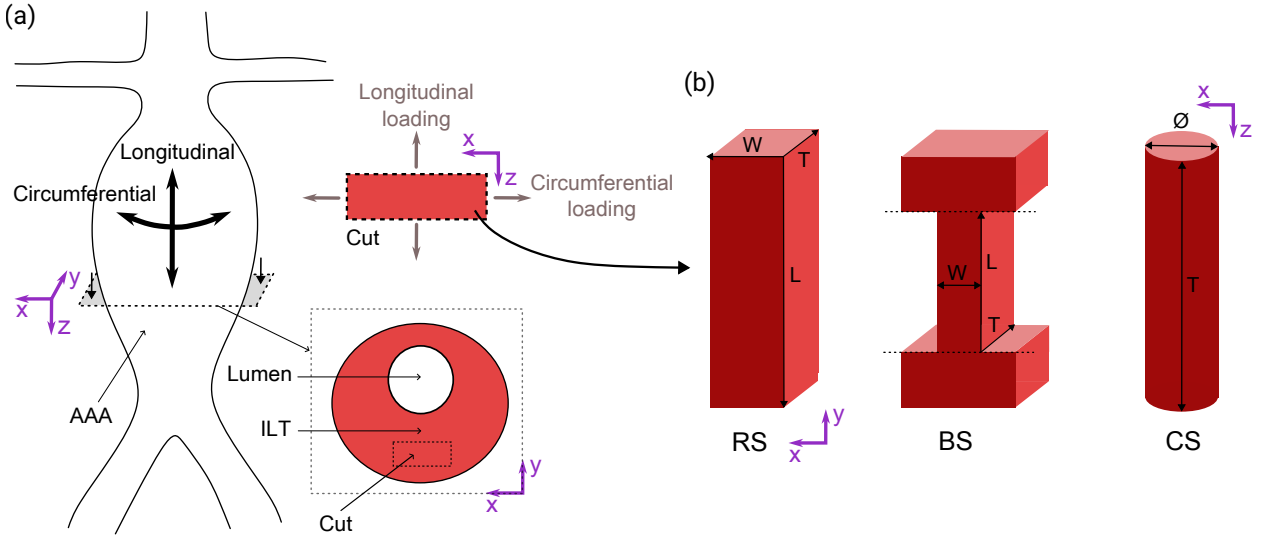

Figure 5: Practical information for mechanical tests on ILT. (a) Schematic representation of the orientation of ILT samples cut for mechanical testing. (b) Geometry description with rectangular-shaped (RS), bone-shaped (BS) and cylindrical-shaped (CS) sample. The letters L, W and T refer to length, width and thickness respectively.

4.1. Uniaxial tensile test (UTT)

The majority of UTT studies were performed until failure (UF) to determine the elastic modulus (E) from 0.05 to 0.27 MPa (46) and/or tensile strength, but also to give information on the failure properties of ILT (see supplementary material 6). Moreover, all studies tested the various ILT layers separately. A study demonstrated a protective role of the ILT in reducing wall stress in AAA (46). This conclusion was affirmed after conducting finite element analysis (FEA) simulations, where the ILT was modeled with a linear material behavior based on their traction results (46). Nevertheless, the simulations were performed on 2D idealized AAA geometries (46). The rest of the studies highlighted the detrimental role of the ILT in the pathology, even if different mechanical behaviors were identified with linearity (34; 47) and non-linearity (25; 48; 49; 50). One of the work that found a linear behavior linked stiff or large ILT to an increased risk of AAA rupture, attributed to the weakening of the aneurysm wall (34). However, as ILT undergoes large *in-vivo* deformation up to 15% (51) under physiological pulse pressure, a linear behavior seems inappropriate (31). Most UTT studies that examined longitudinal (25), circumferential (47; 50; 48), or both directions (27; 49), reported a non-linear behavior, which is attributed to the tissue's hyperelastic properties (31; 47; 50; 25; 49; 48). Many parameters such as the age of ILT or testing conditions can affect the mechanical behavior and the non-linearity was reported at different strains, from 5% (48) to 20% (31; 49) deformation, showing no clear transition. No significant

difference was observed between longitudinal and circumferential orientations for tensile properties of luminal and medial layers (27; 49). Finally, these studies reported ultimate tensile strength (UTS) values ranging from 0.019 to 0.658 MPa, which decreases from the luminal to the abluminal regions and is lower in thick ILT compared to thin ILT. This wide range of UTS values was likely due to differing testing conditions such as loading rate and hydration levels.

Even if the same type of ILT solicitations were conducted for the majority of studies, different strain-stress relationships of ILT were reported with linear and non-linear behaviors. In addition, all studies concluded on an isotropic ILT behavior and some authors developed different constitutive models as summarized in supplementary material 7, that can be used to provide information regarding wall stress distribution in AAA from numerical simulations. The role of ILT varies depending on the model employed in numerical simulations, ranging from protective (46; 52) to detrimental (26). These different findings may be explained first by the variability in biological properties but also by the experimental setup and testing conditions. Other limitations need to be mentioned with the fact that tensile test does not accurately mimic the *in-vivo* loading conditions. Finally, the validity of results obtained through the UTS approach could be called into question given that the latest studies using this technique dates back to 2015 (49; 48), and considerable advancements have occurred in the field since that time.

4.2. Biaxial tensile test (BTT)

Compared to classical UTT, BTT better mimic physiological loading and evaluate potential anisotropy because fibers are implicated. Only three studies conducted BTT on the different ILT layers separately (53; 27; 54). Among these studies, two reported an isotropic behavior (53; 54) (Figure 6) with slightly stiffer samples cut in the longitudinal direction compared to circumferentially-oriented cut samples, but no significant difference was observed (54). The other study observed an anisotropic behavior for one third of the luminal samples (27). The anisotropy may be correlated to the age of the ILT with anisotropic behavior only reported for old ILT, with highly degraded medial and abluminal layers (27). Then, a nearly linear force-strain relationship was identified which is quite unusual for this type of tissue as previously mentioned for UTT results (53). Using the same experimental protocol, another study (27) found a non-linear force-strain relationship was observed, which could be explained by the fact that the tissue was not hydrated during the test modifying its behavior. Finally, all studies identified also a decrease in stiffness from the luminal to the abluminal layers as reported by UTT studies (47; 31; 50).

Compared to UTT, only a few studies conducted BTT to characterize the biomechanical properties of ILT. The same results as for UTT were reported with a luminal layer stiffer than the abluminal. The results can be used to feed the models used in numerical simulations to predict the wall stress within AAA, and make potential correlation with rupture. However, the developed models (53; 27) have not been incorporated into numerical simulations, leaving the experimental results inconclusive regarding the impact of ILT in AAA. Even if BTT allowed to provide new data on the mechanical behavior of ILT, the experiment remains delicate to set up, particularly for cutting and gripping samples. However, certain limitations should be acknowledged when considering BTT studies. This method does not allow for the measurement of the UTS of ILT and does not fully replicate the *in-vivo* loading conditions, particularly those involving compression. Finally, the reliability of results obtained using the BTT method may be questionable, as only three studies have utilized this approach, with the most recent dating back to 2014 (54), despite significant advancements in the field since then.

4.3. Compression test (COT)

Like most soft biological tissues, ILT exhibits viscoelastic behavior. While this property was suggested in the literature (47), it has been rarely characterized in detail in existing studies. ILT undergoes *in-vivo* compressive loads that can induce over 10% deformation due to blood pressure (31). Compared to UTT, unconfined COT results showed stiffer properties from abluminal to luminal layers (32; 55). Moreover, studies highlighted both viscoelastic (55) and poro-viscoelastic (32) behaviors using stress-relaxation (SR) technique, also hypothesized by (47). All samples were tested layer by layer taking into consideration the multilayered ILT aspect (55; 32). Nevertheless, *in-vivo* physiological loading are applied on the three ILT layers simultaneously. Based on this observation, a study performed compression tests on the three layers simultaneously, showing a non-linear viscoelastic behavior with a high intra-patient variability (40).

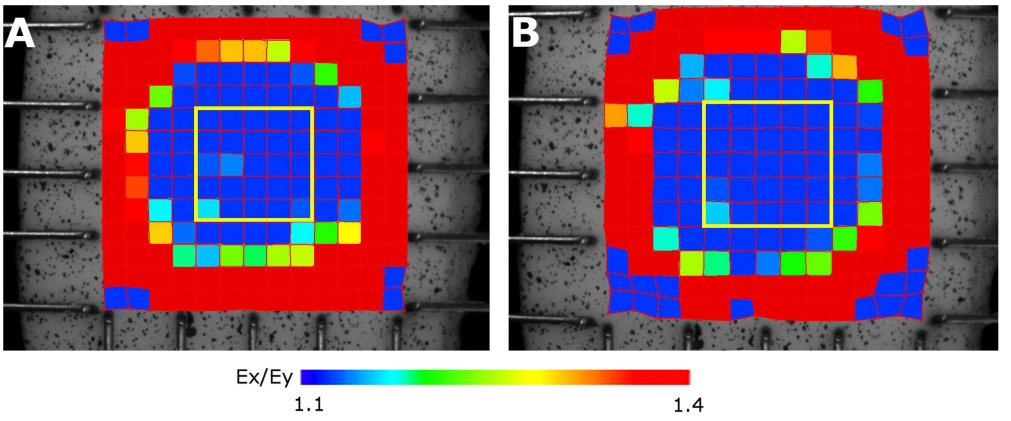

Figure 6: Bi-axial test showing strain comparison using digital image correlation (DIC) between circumferential (Ex) and longitudinal (Ey) directions at deformation of (A) $\lambda = 1.07$ and (B) $\lambda = 1.14$. The blue cells represent the area which can be considered sensibly uniform and free from edge effects (Ex/Ey $\leq$ 1.1) (taken from (54) with permission).

Finally, a study conducted unconfined compression tests on entire ILT samples to investigate the stability of ILT following aneurysm repair using an endovascular aneurysm sealing (EVAS) system (30). They observed a fluid-displacement within ILT leading to a small decrease of volume (30). These results confirmed that ILT is a fluid-permeable porous medium in most cases (29; 26; 24).

Only very few studies conducted unconfined COT bringing new insights concerning the viscoelastic behavior of ILT (55; 32). Moreover, stiffer mechanical properties from abluminal to luminal regions (55; 32) were highlighted unlike UTT results. However, comparing the results is challenging due to the significant differences in deformation ranges, varying from 5%-15% (55) to 45%-55% (32). Only one study developed a constitutive model emphasizing the importance of viscoelasticity in ILT simulations (32), with no direct connection made regarding the role of ILT in vessel wall weakening. Finally, given that physiological loading is applied simultaneously to all three ILT layers, it would be valuable to assess the viscoelastic behavior by testing all layers together.

4.4. Shear test (ST)

As COT, ST were conducted to obtain the viscoelastic behavior of ILT. Using small strain ST experiments, ILT was found to linearly-behaves (56; 57) until 3% strain (56). The results for E (ranging from 15 to 60 kPa) were found to be consistent with UTT studies (31; 46), which reported an approximate value of 50 kPa (31) and a range of 50 to 200 kPa (46). However, the small strain approach was questioned and large strain experiments was performed until 20% strain, demonstrating a non-linear viscoelastic behavior (58). Based on these results, a multi-mode viscoelastic model was developed to describe the linear and the non-linear viscoelastic properties of the ILT (58), but no study used this model in numerical simulations.

ST is a valuable tool to purely obtain the viscoelastic behavior of biological tissues. However, it is complicated to draw conclusion on the ILT influence in AAA as no numerical studies used the developed model. Moreover, only three studies on ILT, all conducted prior to 2010, have been performed. Drawing conclusions from their results is challenging, as two of these studies employed non-physiological deformations. Recently, tools have been utilized to study the viscoelastic behavior of blood clots (59), and conducting similar experiments could offer valuable insights into the mechanistic understanding of ILT.

5. Constitutive ILT models

Constitutive models are essential tools for understanding the mechanical behavior of ILT and so for addressing vascular pathologies effectively. These models provide a mathematical framework to depict the relationship between the mechanical properties of ILT and external forces or deformations that they undergo *in-vivo*. Coming from experimental

studies and presented in supplementary material 7, constitutive models are used in numerical simulations to mimic the pathological behavior of ILT, and evaluate their impact in the pathology.

A first constitutive model of ILT was developed at the end of the 90's by Di Martino *et al.* (1998) with low complexity, describing the mechanical behavior of ILT as an isotropic, incompressible (or quasi-incompressible), linear and elastic material (46). The Hooke's law

$$\sigma = \epsilon E \tag{1}$$

was used to describe the behavior with σ the stress, ϵ the strain and E the Young's Modulus. Since the majority of mechanical studies demonstrated a non-linear behavior, different hyperelastic models were developed. Both UTT (50; 47; 31; 49; 25) and BTT (53; 27) were used identifying the material parameters. Different strain-energy density function (SEDF) were used to described ILT behavior such as Mooney-Rivlin (eq.2), second- (eq.3) and third-order Yeoh (eq.4), and Ogden-type (eq.5)

$$W = c_1(I_1 - 3) + c_2(I_2 - 3), \quad (c_1, c_2, \text{ material parameters from (31)}) \tag{2}$$

$$W = c_1(I_1 - 3) + c_2(I_1 - 3)^2 \quad (c_1, c_2, \text{ material parameters from (53)}) \tag{3}$$

$$W = c_1(I_1 - 3) + c_2(I_1 - 3)^2 + c_3(I_1 - 3)^3 \quad (c_1, c_2, c_3, \text{ material parameters from (50)}) \tag{4}$$

$$W = c \sum_{i=1}^{3} (\lambda_i^4 - 1) \quad (c, \text{ is a material parameter from (47)}) \tag{5}$$

where c refers to material constant, λ refers to the principal stretches, and I_1 and I_2 are first and second invariants of the Cauchy-Green strain tensor. Only one study developed a anisotropic hyperelastic SEDF (eq.6)

$$W = \mu(I_1 - 3) + \frac{k_1}{2.k_2}[e^{k_2(1-\rho)(I_1-3)^2 + k_2\rho(I_4-1)^2} - 1] \quad (\mu, \rho, k_1, k_2, \text{ are material parameters from (27)}) \tag{6}$$

where μ, ρ, k_1 and k_2 are stress-like parameters (27).

The above mentioned hyperelastic models can describe the stress-strain properties of ILT tissue but can not explain the viscoelastic behavior. A study proposed a non-linear viscoelastic behavior of ILT using a multi-mode Maxwell model (58). Since the ILT is assumed to be incompressible, the Cauchy stress can be split into a volumetric σ^v and a deviatoric part σ^d (58). The deviatoric part was split into an elastic part called σ_0^d, and into n viscoelastic modes written as

$$\sigma^d = \sigma_0^d + \sum_{i=1}^{n} \sigma_i^d \tag{7}$$

In eq.(7), the elastic behavior was modeled with

$$\sigma_i^d = G_i B_{e,i}^d \tag{8}$$

where $B_{e,i}^d$ corresponds to the deviatoric part of the elastic Finger tensor B_e of mode i. A non-linear equilibrium mode was added to the viscoelastic modes with a modified Mooney-Rivlin-type

$$\sigma_0^d = 2\frac{\partial W}{\partial I_1} B^d - 2\frac{\partial W}{\partial I_2}(B^{-1})^d \tag{9}$$

where W is the SEDF, I_1 and I_2 the first and the second invariants of the Finger tensor. By developing, σ_0^d was rewritten as

$$\sigma_0^d = G_0[(1-A)\exp(-C\sqrt{bI_1 + (1-b)I_2 - 3}) + A] \times [bB^d - (1-b)(B^{-1})^d] \tag{10}$$

with A and C material parameters that describe the non-linear behavior (27). Only one study identified a poro-viscoelastic behavior, that may significantly influence fluid transport from the lumen to the aortic tissue (32). Considering the ILT composed of two phases: solid (V_s) and fluid (V_f) (Figure 7) as described in the Biot consolidation theory (60), they modeled the viscous behavior of the solid phase with the Kelvin form of the standard linear solid (SLS) model, while introducing the permeability k in the Biot consolidation equations (32).

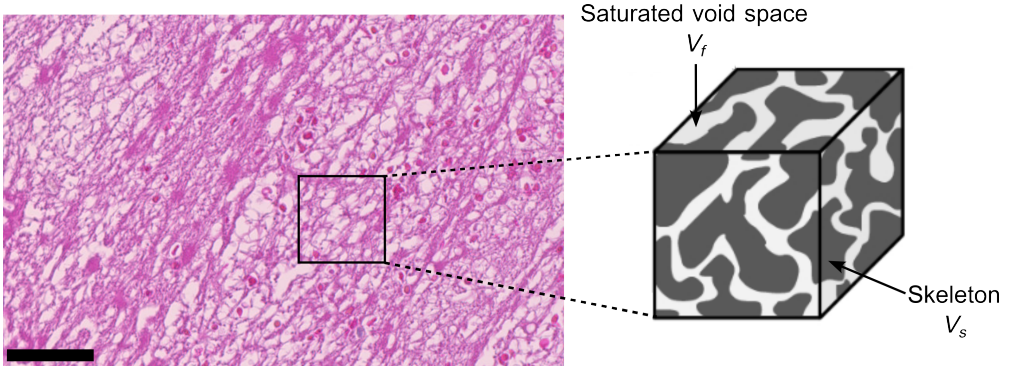

Figure 7: Illustration of the porous theory used to described the ILT behavior. Histological section of the medial layer showing pores in white and matter in pink (taken from (29) with permission) [**Note: I am an author of this article; Copyright: CC BY-NC-ND 4.0**, permission pending from Taylor & Francis**]. On the right, a representative elementary volume (REV) of the ILT is taken with both solid skeleton and porous saturated space with fluid. The scale bar is 50 μm.

A wide range of constitutive models was developed in order to catch the ILT behavior. The commonly employed models are primarily hyperelastic, enabling the representation of the non-linear characteristics of ILT. Moreover, these models may be used to investigate stress analysis in AAA with ILT (26), directly estimate wall stress in AAA, and predict potential rupture (58; 31; 26; 53). However, some studies highlighted the importance of poroelasticity (32) and viscoelasticity (32; 56; 57; 58) to better predict AAA wall rupture risk. Numerical studies utilizing poroelastic (61) or porohyperelastic (62) models demonstrated that ILT tends to reduce wall stress in AAA. They underscored the importance of considering the porous properties of ILT, including biochemical transport processes such as oxygen delivery. Only a limited number of studies explored these crucial properties, employing various experimental setups and yielding diverse results. Lastly, there are limitations associated with the testing protocol, as well as the fact that most models are based on luminal testing only, which cannot accurately represent the physiological ILT behavior.

6. Conclusion and perspectives

Various approaches have been employed to enhance the understanding of the morphological and mechanical properties of thrombus within AAA and their impact on the pathology. *In-vivo* investigations provided morphological insights into the heterogeneous, porous ILT structure, highlighting the presence of specific hypoxia markers that may affect vessel wall integrity and contribute to rupture. On the other hand, the scarcity of human samples and the number of *ex-vivo* morphological studies are highly limited. Although the ILT microstructure has been 2D- and 3D-imaged at cellular resolution, highlighting the significance of its porous structure in transmitting cells and nutrients to the aortic wall, questions remain about how cells navigate within this medium and play a role in AAA evolution. The ILT mechanical behavior was also investigated through several techniques with a common answer that ILT behaves as a non-linear material. However, unlike arterial wall (63), there is no standard protocol for thrombi testings, which introduces challenges in comparing and interpreting results. Crucial parameters when conducting mechanical test such as sample freshness or hydration are not always respected questioning the results as well. Furthermore, the use of a simple hyperelastic model may be insufficient, as key parameters such as poroelasticity and viscoelasticity must also be considered, as they play a crucial role in the time-dependent responses of biological tissues (64). Moreover, some hallmark features of poroelasticity have been highlighted experimentally with permeability gradients and fluid transport but are not accurately incorporated into existing models. Finally, only one study assessed ILT age and demonstrated that the mechanical properties of ILT may change significantly with age (27), highlighting the importance of considering ILT age in AAA-related research. High morphological and mechanical heterogeneities were observed in the ILT, raising the question of which model is most relevant and whether the influence of thrombus age should be incorporated into the model. Developing a reliable ILT model is essential, as it significantly influences numerical outcomes.

Future perspectives must be explored to address the remaining unanswered questions. The advancement of imaging tools, such as phase-contrast micro/nano-tomography, opens opportunities for new studies to delve deeper into the ILT's microstructure and composition. These techniques enable the acquisition of 3D morphology with nanometric spatial resolution, offering valuable insights into fluid and cell navigation mechanisms within this complex, heterogeneous porous medium. Concerning the mechanical characterization, the development of standardized protocols will facilitate the straightforward comparison of ILT properties. Moreover, *in-situ* mechanical testing may be conducted under X-rays micro-CT in order to directly link microstructure and mechanical properties of ILT. Then, better investigations of ILT viscoelasticity and poroelasticty with appropriate tests (59) may bring new insights concerning the mechanical responses of ILT. A wide range of mechanical parameters emerged from the experiments, but new multi-solicitation tests could be beneficial for identifying the most important parameters. Further investigations are needed on ILT modeling, considering whether to include ILT evolution/remodeling, as its properties undergo significant changes over time and with age. A need in longitudinal studies is also required to correlate numerical models and AAA evolution that include ILT. As one of the consequences of the presence of ILT would be the rupture of the vessel, further studies might compare morphological and mechanical ILT properties between non-ruptured and ruptured AAA to potentially make some correlations (size, microstructure, mechanics, composition, etc.). Finally, studies on aortic thrombi from dissections should be conducted on human subjects to: (1) assess both macroscopic and microscopic properties, (2) compare these properties with other aortic thrombi such as ILT, and (3) gain a deeper understanding of their formation and role in the progression of the pathology.

Authors' contributions

JL and VD conceived the outline of this manuscript; JL retrieved the literature; JL wrote the original draft; JL, JV and VD edited and revised the manuscript; JL, JV and VD approved the final version of this manuscript.

Acknowledgments

We would like to thank the Department of Vascular Surgery of the Timone Hospital and more particularly Mariangela De Masi, M.D., for providing the human ILT samples.

Disclosure statement

The Research Ethics Committee approved the use of human ILT by our group (No. XJFXL8) as shown in Figures 2, 4 and 7.

Data availability statement

The authors confirm that the data supporting the findings of this study are available within the article.

Funding

This work was supported in part by an IMI project grant - Institut Mécanique et Ingénierie (IMI) - Initiative d'Excellence d'Aix-Marseille Université - A*MIDEX (AMX-19-IET-010).

Conflict of interest

The authors declare that the research was conducted in the absence of any commercial or financial relationships that could be construed as a potential conflict of interest.

Appendices

Supplementary material 1: Summary table of MRI studies performed on human *in-vivo* ILT from AAA.

Supplementary material 2: Summary table of histological studies performed on human *ex-vivo* ILT from AAA.

Supplementary material 3: Summary table of SEM studies performed on human *ex-vivo* ILT from AAA.

Supplementary material 4: Summary table of micro-CT studies performed on human *ex-vivo* ILT from AAA.

Supplementary material 5: Summary table of values at break of *ex-vivo* ILT using UTT. The mean UTS are expressed in MPa. The subscripts L and C refer to the sample orientation with longitudinal and circumferential directions, respectively.

Supplementary material 6: Summary table of mechanical experiments performed on human *ex-vivo* ILT from AAA.

Supplementary material 7: Summary table of ILT constitutive models.

Table 1
Summary of MRI studies performed on human in-vivo ILT from AAA.

Ref.	NP	Equipment	Method	Main findings
(23)	15	1.5-T system	• T2-weighted TSE sequences (non breath hold) of the entire abdominal cavity • T1- and T2*-weighted GRE sequences (breath hold) of the entire abdominal cavity • Same procedure after 1h of SPIO staining (0.075 mL/kg) • T2*-, T2- and T1-weighted sequences of *ex-vivo* ILT	• T2-weighted images show a multilayered thrombus in most cases • Quantitative SNR values from *in-vivo* T2-weighted images with 28.6 and 37.1 for luminal and deeper ILT respectively (without SPIO). Increase of SNR with SPIO with 30.6 and 40.2 for luminal and deeper thrombus respectively • *Ex-vivo* T2-weighted images show a low signal intensity at the luminal layer • Linear correlation between thrombus signal decrease and the quantity of platelets and MMPs
(19)	*	1.5-T system	• 3D FGRE sequences to localize the AAA • T2-weighted TSE (breath hold) of the AAA • T1-weighted GRE of the AAA	• Visualization of ILT internal structure (different layers) with T2-weighted images • Distinction between organized (mostly solid) and minimally organized (mostly fluid) ILT structures • Internal structure visible with MRI compared to CT and US
(20)	34	1.5-T system	• T1-weighted GRE (breath hold) on the AAA • T1-weighted TSE (non breath hold) on the AAA • T2-weighted TSE (breath hold) on the AAA • T1-weighted TSE after 5min of Gadobutrol staining (0.1 mL/kg)	3 ILT categories based on T2-weighted sequences where category 1 corresponds to a solid ILT with an homogeneous appearance, category 2 with a disintegrated ILT with a thin layer of luminal and category 3 that corresponds to a largely solid ILT with a multilayered heterogeneous appearance
(22)	35	1.5-T system	• 3D T1-weighted TFE of AAA • 3D T1-weighted TFE with Gadobutrol staining (0.1 mmol/kg) • Follow-up with the same procedure after 2 weeks, 6 months and 12 months	• High SIR in ILT is associated with a higher aneurysm growth rate. AAAs grow two times faster with fresh ILT compared to AAAs without fresh ILT • High SIR corresponds to unorganized loose thrombus structure
(21)	26	3-T system	• 3D T1-weighted black blood (FSE) with blood suppression preparation sequences of the coronal plane of the AAA • 3D T1-weighted FGRE of the AAA	• ILT internal structures with T1-weighted images • 3D black blood sequences more reliable for ILT characterization compared to gradient-echo sequences

CT: Computed Tomography; FGRE: Fast Gradient Recalled Echo; FSE: Fast Spin Echo; GRE: Gradient Recalled Echo; MMP: Matrix Metalloproteinases; NP: Number of Patient; SIR: Signal Intensity Ratio; SNR: Signal to Noise Ratio; SPIO: SuperParamagnetic Iron Oxide; T1-weighted: Highlights the differences in the longitudinal relaxation time (T1) of tissues, T2-weighted: Emphasizes the differences in the transverse relaxation time (T2) of tissues; TFE: Turbo Fast Echo; TSE: Turbo Spin Echo; US: Ultrasounds; *: No information.

Table 2
Summary of histological studies performed on human *ex-vivo* ILT from AAA.

Ref.	NP	NS	Staining techniques	Main findings
(24)	24	24	• HE • IHC: CD4; CD8	• Networks of connected canaliculi with areas that increase from luminal (62.3 μm^2) to abluminal (275.9 μm^2) layer • Number of macrophages decreases from 85.6 (luminal) to 3.7 (abluminal)
(28)	7	20	• HE • IHC: vWF; Hoescht; ORP; CD45	• ILT leads to hypoxia because of the high amount of inflammatory cells (1.5%<WBC<3%) and ORP expression • Difference in neovascularization within AAA wall with and without ILT
(26)	7	105	Picro-Sirius Red	• Larger pores in abluminal layer compared to luminal and medial layers • Mean porosity of 23.28% (luminal), 22.91% (medial) and 19.59% (abluminal)
(27)	43	32	HE; PBL; EvG; SFOG	Four-phase ILT evolution. Phase I with RBCs only and few loose fibrin network. Phase II with loose fibrin network and less cellular elements. Phase III with more condensed network with thick bundles. Phase IV with condensed fibrin and no cellular elements • Decrease in RBC concentration with age (from 80% to 0%)
(36)	*	*	• HE • IHC: CD66b	• Luminal layer is composed by cell-rich fibrin (RBCs) • Presence of neutrophils in the luminal layer • High proteolytic activity
(25)	*	8	HE; SFOG	• Increase of collagen network from luminal to abluminal layer • Circumferential alignement of canaliculi in the luminal layer • Increase of pore sizes from luminal to abluminal layer ($\approx$ 300 μm) • Cell penetration limited to the medial
(30)	4	*	HE	• The fluid inside canaliculi in the medial layer decrease between 50% to 96% after compression • Fragmentation of abluminal layer after compression (200mmHg) • Change of volume may explained EVAS issues
(29)	4	16	• HE • IHC: CD61	• Luminal layer is composed by RBCs, leukocytes and platelets in loose fibrin network • Medial layer shows agglomerated RBCs in pores with low concentration of platelets • No porosity in the abluminal layer with low concentration of platelets

HE: Hematoxylin and Eosin; IHC: ImmunoHistoChemistry; vWF: von Willebrand Factor; ORP: Oxygen-Regulated Protein; PBL: Prussian BLue; EvG: Elastica van Gieson; SFOG: Mallory-Cason Trichrome.

Table 3
Summary of SEM studies performed on human *ex-vivo* ILT from AAA.

Ref.	NP	Sample preparation	Main findings
(24)	7	• Washing (PBS) • Fixation (2.5% glutaraldehyde in PBS) • Embedding (mercox resin) • Washing (20% NaOH then PBS) • Dehydration (ethanol) • Coating (gold-palladium)	Continuous network of interconnected canaliculi through the thrombus and validation of histological hypothesis of interconnected channels
(31)	*	• Washing (PBS) • Fixation (2% paraformaldehyde in PBS) • Cutting • Fixation (1% OsO_4) • Dehydration • Drying (critical point) • Coating (gold)	• Structural differences between all 3 layers • Luminal layer with thick bundles of fibrin fibers and secondary finer cross-linked structures with cells • Medial layer shows degenerated fibrin fibers in some regions • Abluminal layer with no structure, totally degenerated fibers with less viable cells
(32)	1	*	Inhomogeneous porous structure with different pore sizes through the thickness explained by successive layer formation
(33)	1	• Washing (PBS) • Fixation (2.5% glutaraldehyde in PBS) • Dehydration (alcohol) • Coating (gold)	• Patient-specific structure of ILT • Luminal layer is composed by high amount of fibrin fibers with irregular shapes and cellular elements (RBCs, platelets, etc.) • Abluminal layer composed of dense fibrin fibers with pores ($\varnothing$ 1-2 μm) and very low amount of RBCs
(34)	15	• Fixation (100% methanol) • Washing (100% ethanol) • Dehydration (gradual ethanol up to 100%) • Drying (gradual hexamethyldisilazane from 50% to 100%) • Coating (gold)	• Four ILT types: (1) fresh with only luminal, (2) disintegrated with thin solid layer at luminal surface, (3) bi-layered with luminal and medial, (4) multilayered with the 3 layers • Circumferential orientation of fibrin in luminal region for types (1) and (3) • No apparent structure and pore in type (4) ILT • Presence of calcifications in AAA wall with ILT

PBS: Phosphate Buffered Saline solution.

Table 4
Summary of micro-CT studies performed on human *ex-vivo* ILT from AAA.

Ref.	NP	Technique	Sample preparation	Resolution	Main findings
(29)	4	CE-MCT	• Fixation (10% formalin) • Dehydration (alcohol) • Staining (PTA)	3 μm	• Inhomogeneous structure with porosity gradients through ILT thickness • The porosity, the mean pore diameter and the mean distance between pores are obtained for all 3 layers showing that luminal ($\phi = 7.4\%$) and medial ($\phi = 8.2\%$) layers are more porous than abluminal ($\phi = 4\%$) layer • Microscopic permeability of the luminal layer is $3.79 \times 10^{-14} m^2$ • Agreement between macroscale and microscale results
(40)	2	CE-MCT	Staining (SPT)	3 μm	• Tissue preservation using SPT staining • Higher porosity and lower pore diameter values compared to PTA staining with porosity of 13.2%, 13% and 4.3% for luminal, medial and abluminal layers respectively • Preparation protocol validated for *in-situ* mechanical tests

CE-MCT: Contrast-Enhanced Micro-Computed Tomography; PTA: PhosphoTungstic Acid; SPT: Sodium PolyTungstate.

Table 5
Summary of mechanical experiments performed on human *ex-vivo* ILT from AAA.

Test	AP	NP	NS	DUS	TT	Bath/Temp	Preconditionning	Strain	Loading	Ref.
UTT	71.8	6	21	22x4x3.6 (BS)	24h	-; 23°C	-	UF	0.33 $mm.s^{-1}$	(46)
	69	14	50	10x2x0.6 (RS)	24h	-; *	NPC=10 to 10% strain at 0.008 $mm.s^{-1}$	UF	0.008 $mm.s^{-1}$	(31)
	72.4	8	112	30x4x1.5 (BS)	*	DMEM; 37°C	-	UF	0.2 $mm.s^{-1}$	(47)
	65	1	7	35x6x2.3 (RS)	24h	Saline; RT	NPC=10 to 2.9% strain	UF	0.1 $mm.s^{-1}$	(50)
	*	4	8	60x18x* (RS)	12h	-; 37°C	NPC=3 but *	UF	*	(25)
	*	11	15	*x1.5x* (RS)	*	Saline; 37°C	NPC=5 to 5% strain at 0.05 $mm.s^{-1}$	UF	0.01 $mm.s^{-1}$	(49)
	71.8	12	15	22x4x* (RS)	48h	Saline; 37°C	NPC=10 to 7% strain at 0.03 $mm.s^{-1}$	UF	*	(48)
	72	15	114	* (RS)	*	*;*	NPC=9 to 25% strain at 12.5% of the gauge $length.s^{-1}$	25%	12.5% of the gauge $length.s^{-1}$	(34)
BTT	71	9	9	20x20x2.08 (RS)	48h	-; 23°C	NPC=9 but *	SC; maximum tension without damaging	40 $N.m^{-1}$; RoT=1:1; 0.75:1; 1:0.75; 0.5:1; 1:1	(53)
	67	43	67	20x20x2.57 (RS)	6h	DMEM; 37°C	NPC=10 but *	SC; *	*; RoT=1:1; 0.75:1; 1:0.75; 0.5:1; 1:1	(27)
	71.2	19	356	14x14x* (RS)	*	Saline; 37°C	NPC=10 to 20% (of gripped area) at 0.2 $mm.s^{-1}$	DC; 20%	0.2 $mm.s^{-1}$; α=1:1	(54)

AP: Mean Age of Patient; BS: Bone-Shaped sample; CS: Cylindrical-Shaped sample; DC: Deformation-Controlled; DMEM: Dulbecco's Modified Eagle's Medium; DUS: Dimension of Unloaded Sample; NP: Number of Patient; NPC: Number of Preconditioning Cycle; NS: Number of Sample; RoT: Ratio of Tension; RS: Rectangular-Shaped sample; RT: Room Temperature; SC: Stress-Controlled; TT: Maximum Elapsed Time between harvesting and Test; UF: Until Failure; *: No information; -: Not used.

Test	AP	NP	NS	DUS	TT	Bath/Temp	Preconditionning	Strain	Loading	Ref.
COT	*	8	49	⌀ 7x1 (CS)	*	-; *	-	SR; PC at 40% then 45, 50, 55% (RX=2h)	0.01 $mm.s^{-1}$	(32)
	72.5	6	47	⌀ 8x3.98 (CS)	48h	PBS; 37°C	-	SR; 5, 10, 15% (RX=20 min)	PL=0.02 N; *	(55)
	70	21	21	Full	*	-; *	-	*	200 mmHg for 5 min; *	(30)
	60	2	6	* (RS)	*	-; *	NPC=5 to 40% at 0.0295 $mm.s^{-1}$ (for 2 samples)	0 to 40% (1 LUC)	0.0295 $mm.s^{-1}$	(40)
ST	*	6	17	• ⌀ 10/14x2 (CS) • ⌀ 10x0.5 (CS)	24h	-; RT/37°C	-	*	0.1 to 100 $rad.s^{-1}$	(56)
	*	6	10	18x18x2.5-4 (RS)	14j	Saline; *	NPC=4 but *	1%	5, 6.3, 9.4, 24.5 $rad.s^{-1}$	(57)
	*	7	13	⌀ 10x0.4-0.6 (CS)	*	PBS; 37°C	• SD: - • LD: -	• SD: 3% (constant) • LD: SR at 1, 5, 10, 15, 20% (RX=10s)	• SD: 6.3 to 628.3 $rad.s^{-1}$ • LD: 1 s^{-1}	(58)

AP: Mean Age of Patient; CS: Cylindrical-Shaped sample; DC: Deformation-Controlled; DUS: Dimension of Unloaded Sample; LD: Large Deformation; LUC: Loading-Unloading Cycle; NPC: Number of Preconditioning Cycle; NP: Number of Patient; NS: Number of Sample; PBS: Phosphate Buffered Saline solution; PC: Pre-Conditioned; PL: Pre-Load; RS: Rectangular-Shaped sample; RT: Room Temperature; RX: Relaxation Time; SC: Stress-Controlled; SD: Small Deformation; SR: Stress-Relaxation Test; TT: Maximum Elapsed Time between harvesting and Test; *: No information; -: Not used.

Table 6
Summary of values at break of ex-vivo ILT using UTT. The mean UTS are expressed in MPa. The subscripts L and C refer to the sample orientation with longitudinal and circumferential directions, respectively. *: no information.

References	Mean UTS (SD)	Mean maximum deformation (SD)
(46)	ILT: 0.085 (0.047)	ILT: 0.636 (0.187)
(31)	• Luminal_L: 0.520 (0.070) • Luminal_C: 0.540 (0.070) • Medial_L: 0.300 (0.070) • Medial_C: 0.220 (0.050)	*
(47)	• Luminal: 0.157 (0.058) • Medial: 0.092 (0.038) • Abluminal: 0.048 (0.023)	*
(50)	ILT: 0.019 (0.013)	ILT: 0.369 (0.157)
(25)	*	*
(49)	• ILT_L: 0.080(*) • ILT_C: 0.051 (*)	• ILT_L: 0.628 (*) • ILT_C: 0.352 (*)
(48)	• ILT_{thin}: 0.658 (0.325) • ILT_{thick}: 0.320 (0.141)	*

Table 7
Summary of ILT constitutive models identified in experiments.

Row	Ref.	Methods	Models	Key equations
1	(46)	UTT	Homogeneous; isotropic; linear; elastic (Hooke)	$\sigma = \varepsilon E$
2	(53)	BTT	Isotropic; incompressible; hyperelastic (Yeoh)	$W = c_1(I_1 - 3) + c_2(I_1 - 3)^2$
3	(50)	UTT	Homogeneous; isotropic; incompressible; hyperelastic (Yeoh)	$W = c_1(I_1 - 3) + c_2(I_1 - 3)^2 + c_3(I_1 - 3)^3$
4	(47)	UTT	Isotropic; incompressible; hyperelastic (Ogden-type)	$W = c \sum_{i=1}^{3} (\lambda_i^4 - 1)$
5	(31)	UTT	Isotropic; incompressible; hyperelastic (Mooney-Rivlin)	$W = c_1(I_1 - 3) + c_2(I_2 - 3)$
6	(49)	UTT	Isotropic; incompressible; hyperelastic (modif. Mooney-Rivlin)	$W = c_1(I_1 - 3) + D_1[e^{D_2(I_1-3)} - 1] + K(J - 1)$
7	(25)	UTT	Isotropic; incompressible; hyperelastic	$W = \sum_{i+j=1}^{n} c_{ij}(I_1 - 3)^i(I_2 - 3)^j + \frac{1}{d}(J - 1)$
8	(27)	BTT	• Isotropic; hyperelastic • Anisotropic; hyperelastic	• $W = \mu(I_1 - 3) + \frac{k_1}{2.k_2}[e^{k_2(I_1-3)^2} - 1]$ • $W = \mu(I_1 - 3) + \frac{k_1}{2.k_2}[e^{k_2(1-\rho)(I_1-3)^2 + k_2\rho(I_4-1)^2} - 1]$
9	(56)	ST	Linear; viscoelastic (Maxwell)	• $G' = \sum_{i=1}^{n} G_i \frac{\lambda_i^2\omega^2}{1+\lambda_i^2\omega^2}$ • $G'' = \sum_{i=1}^{n} G_i \frac{\lambda_i\omega}{1+\lambda_i^2\omega^2}$
10	(58)	ST	Non-linear; viscoelastic (multi-mode Maxwell)	• $\sigma^d = \sigma_0^d + \sum_{i=1}^{n} \sigma_i^d$ • $\sigma_i^d = G_i B_{e,i}^d$ • $\sigma_0^d = 2\frac{\partial W}{\partial I_1} B^d - 2\frac{\partial W}{\partial I_2}(B^{-1})^d$
11	(32)	COT	Poroviscoelastic	$\sigma'(t) = D^{ve} \cdot \epsilon^{ve}(t) + V^{ve} \cdot \epsilon^{ve}$

References

[1] Q. Mattingly, "Cardiovascular diseases – overview," 2024. https://www.who.int/health-topics/cardiovascular-diseases#tab=tab_1.

[2] J. Golledge, "Abdominal aortic aneurysm: update on pathogenesis and medical treatments," *Nature Reviews Cardiology*, vol. 16, no. 4, pp. 225–242, 2019.

[3] B. Liu, D. J. Granville, J. Golledge, and Z. Kassiri, "Pathogenic mechanisms and the potential of drug therapies for aortic aneurysm," *American Journal of Physiology-Heart and Circulatory Physiology*, vol. 318, no. 3, pp. H652–H670, 2020.

[4] M. Landenhed, G. Engström, A. Gottsäter, M. P. Caulfield, B. Hedblad, C. Newton-Cheh, O. Melander, and J. G. Smith, "Risk profiles for aortic dissection and ruptured or surgically treated aneurysms: a prospective cohort study," *Journal of the American Heart Association*, vol. 4, no. 1, p. e001513, 2015.

[5] S. D. Kurz, V. Falk, J. Kempfert, M. Gieb, T. Ruschinski, M. Kukucka, M. Tsokos, H. Grubitzsch, H. Herbst, J. Semmler, *et al.*, "Insight into the incidence of acute aortic dissection in the german region of berlin and brandenburg," *International journal of cardiology*, vol. 241, pp. 326–329, 2017.

[6] E. S. Wise, K. M. Hocking, and C. M. Brophy, "Prediction of in-hospital mortality after ruptured abdominal aortic aneurysm repair using an artificial neural network," *Journal of vascular surgery*, vol. 62, no. 1, pp. 8–15, 2015.

[7] D. Levy, S. Sharma, Y. Grigorova, F. Farci, and J. Le, "Aortic dissection," *StatPearls*, 2024.

[8] M. R. Bersi, V. A. Acosta Santamaría, K. Marback, P. Di Achille, E. H. Phillips, C. J. Goergen, J. D. Humphrey, and S. Avril, "Multimodality imaging-based characterization of regional material properties in a murine model of aortic dissection," *Scientific reports*, vol. 10, no. 1, p. 9244, 2020.

[9] L. E. Schepers, I. N. Chernysh, C. K. Albrecht, L. C. Browning, M. L. Hillsdon-Smith, A. D. Cox, J. W. Weisel, and C. J. Goergen, "Aortic dissection detection and thrombus structure quantification using volumetric ultrasound, histology, and scanning electron microscopy," *JVS-Vascular Science*, vol. 4, p. 100105, 2023.

[10] K. Bäumler, E. H. Phillips, N. Grande Gutiérrez, D. Fleischmann, A. L. Marsden, and C. J. Goergen, "Longitudinal investigation of aortic dissection in mice with computational fluid dynamics," *Computer Methods in Biomechanics and Biomedical Engineering*, pp. 1–14, 2023.

[11] W. R. Wilson, K. H. McCusker, S. M. Peeran, and P. J. Dourdoufis, "Endovascular removal of a large free-floating thrombus of the descending thoracic aorta using the angiovac system," *Journal of Vascular Surgery Cases, Innovations and Techniques*, vol. 10, no. 3, p. 101460, 2024.

[12] G. Li, Y. Chen, H. Wang, Y. Liu, H. Liu, H. Sun, and Z. Wang, "Case report: Surgical strategies of a giant thrombus from the ascending aorta to the arch," *Frontiers in Cardiovascular Medicine*, vol. 10, p. 1091303, 2023.

[13] N. M. Neves, S. C. Coelho, N. F. Marto, and A. B. Horta, "Ascending aortic thrombus with peripheral embolization," *Cureus*, vol. 14, no. 9, 2022.

[14] B. Wang, D. Ma, D. Cao, and X. Man, "Huge thrombus in the ascending aorta: a case report and literature review," *Journal of Cardiothoracic Surgery*, vol. 14, pp. 1–4, 2019.

[15] A. J. Boyd, "Intraluminal thrombus: Innocent bystander or factor in abdominal aortic aneurysm pathogenesis?," *JVS-Vascular Science*, vol. 2, pp. 159–169, 2021.

[16] B. Furie and B. C. Furie, "Mechanisms of thrombus formation," *New England Journal of Medicine*, vol. 359, no. 9, pp. 1449–1461, 2008.

[17] V. Deplano and J.-M. Fullana, *Biological Flow in Large Vessels*. Wiley, 2022.

[18] J. Biasetti, F. Hussain, and T. C. Gasser, "Blood flow and coherent vortices in the normal and aneurysmatic aortas: a fluid dynamical approach to intra-luminal thrombus formation," *Journal of The Royal Society Interface*, no. 63, pp. 938–949, 2011.

[19] F. Labruto, L. Blomqvist, and J. Swedenborg, "Imaging the intraluminal thrombus of abdominal aortic aneurysms: techniques, findings, and clinical implications," *Journal of Vascular and Interventional Radiology*, vol. 22, no. 8, pp. 1069–1075, 2011.

[20] L. de la Motte, M. M. Pedersen, C. Thomsen, K. Vogt, T. V. Schroeder, and L. Lonn, "Categorization of aortic aneurysm thrombus morphology by magnetic resonance imaging," *European journal of radiology*, vol. 82, no. 10, pp. e544–e549, 2013.

[21] C. Zhu, B. Tian, J. R. Leach, Q. Liu, J. Lu, L. Chen, D. Saloner, and M. D. Hope, "Non-contrast 3d black blood mri for abdominal aortic aneurysm surveillance: comparison with ct angiography," *European radiology*, vol. 27, pp. 1787–1794, 2017.

[22] V. Nguyen, T. Leiner, F. Hellenthal, W. Backes, M. Wishaupt, R. Van der Geest, S. Heeneman, M. Kooi, and G. Schurink, "Abdominal aortic aneurysms with high thrombus signal intensity on magnetic resonance imaging are associated with high growth rate," *European Journal of Vascular and Endovascular Surgery*, vol. 48, no. 6, pp. 676–684, 2014.

[23] A. Nchimi, O. Defawe, D. Brisbois, T. K. Broussaud, J.-O. Defraigne, P. Magotteaux, B. Massart, J.-M. Serfaty, X. Houard, J.-B. Michel, *et al.*, "Mr imaging of iron phagocytosis in intraluminal thrombi of abdominal aortic aneurysms in humans," *Radiology*, vol. 254, no. 3, pp. 973–981, 2010.

[24] R. Adolph, D. A. Vorp, D. L. Steed, M. W. Webster, M. V. Kameneva, and S. C. Watkins, "Cellular content and permeability of intraluminal thrombus in abdominal aortic aneurysm," *Journal of vascular surgery*, vol. 25, no. 5, pp. 916–926, 1997.

[25] S. Celi, P. Losi, and S. Berti, "Investigation on regional variation of intraluminal thrombus: a mechanical and histological study," *Bioinspired, Biomimetic and Nanobiomaterials*, vol. 1, no. 3, pp. 183–194, 2012.

[26] T. C. Gasser, G. Martufi, M. Auer, M. Folkesson, and J. Swedenborg, "Micromechanical characterization of intra-luminal thrombus tissue from abdominal aortic aneurysms," *Annals of biomedical engineering*, vol. 38, pp. 371–379, 2010.

[27] J. Tong, T. Cohnert, P. Regitnig, and G. A. Holzapfel, "Effects of age on the elastic properties of the intraluminal thrombus and the thrombus-covered wall in abdominal aortic aneurysms: biaxial extension behaviour and material modelling," *European journal of vascular and endovascular surgery*, vol. 42, no. 2, pp. 207–219, 2011.

[28] D. A. Vorp, P. C. Lee, D. H. Wang, M. S. Makaroun, E. M. Nemoto, S. Ogawa, and M. W. Webster, "Association of intraluminal thrombus in abdominal aortic aneurysm with local hypoxia and wall weakening," *Journal of vascular surgery*, vol. 34, no. 2, pp. 291–299, 2001.

[29] J. Léonet, M. Baudouard, M. de Masi, C. Guivier-Curien, E. Bertrand, H. Lepidi, J. Vicente, and V. Deplano, "Morphological and poro-mechanical characterization of thrombi from aortic aneurysm," in *47ème Congrès de la société de biomécanique*, pp. S5186–S5188, 2022.

[30] K. van Noort, R. C. Schuurmann, B. Wermelink, C. H. Slump, K. C. Kuijpers, and J.-P. P. de Vries, "Fluid displacement from intraluminal thrombus of abdominal aortic aneurysm as a result of uniform compression," *Vascular*, vol. 25, no. 5, pp. 542–548, 2017.

[31] D. H. Wang, M. Makaroun, M. W. Webster, and D. A. Vorp, "Mechanical properties and microstructure of intraluminal thrombus from abdominal aortic aneurysm," *J. Biomech. Eng.*, vol. 123, no. 6, pp. 536–539, 2001.

[32] F. Boschetti, E. Di Martino, and G. Gioda, "A poroviscoelastic model of intraluminal thrombus from abdominal aortic aneurysms," in *Summer Bioengineering Conference*, vol. 47985, pp. 191–192, American Society of Mechanical Engineers, 2007.

[33] P. Matusik, P. Mazur, E. Stępień, R. Pfitzner, J. Sadowski, and A. Undas, "Architecture of intraluminal thrombus removed from abdominal aortic aneurysm," *Journal of thrombosis and thrombolysis*, vol. 30, pp. 7–9, 2010.

[34] H. E. Barrett, E. M. Cunnane, H. Hidayat, J. M. O'Brien, M. A. Moloney, E. G. Kavanagh, and M. T. Walsh, "On the influence of wall calcification and intraluminal thrombus on prediction of abdominal aortic aneurysm rupture," *Journal of vascular surgery*, vol. 67, no. 4, pp. 1234–1246, 2018.

[35] K. Keklikoglou, C. Arvanitidis, G. Chatzigeorgiou, E. Chatzinikolaou, E. Karagiannidis, T. Koletsa, A. Magoulas, K. Makris, G. Mavrothalassitis, E.-D. Papanagnou, *et al.*, "Micro-ct for biological and biomedical studies: A comparison of imaging techniques," *Journal of imaging*, vol. 7, no. 9, p. 172, 2021.

[36] J.-B. Michel, J.-L. Martin-Ventura, J. Egido, N. Sakalihasan, V. Treska, J. Lindholt, E. Allaire, U. Thorsteinsdottir, G. Cockerill, and J. Swedenborg, "Novel aspects of the pathogenesis of aneurysms of the abdominal aorta in humans," *Cardiovascular research*, vol. 90, no. 1, pp. 18–27, 2011.

[37] E. Karagiannidis, N. V. Konstantinidis, G. Sofidis, E. Chatzinikolaou, and G. Sianos, "Rationale and design of a prospective, observational study for the quantitative estimation of thrombus burden in patients with st-elevation myocardial infarction using micro-computed tomography: The quest-stemi trial," *BMC Cardiovascular Disorders*, vol. 20, pp. 1–8, 2020.

[38] E. Karagiannidis, A. S. Papazoglou, G. Sofidis, E. Chatzinikolaou, K. Keklikoglou, E. Panteris, A. Kartas, N. Stalikas, T. Zegkos, F. Girtovitis, *et al.*, "Micro-ct-based quantification of extracted thrombus burden characteristics and association with angiographic outcomes in patients with st-elevation myocardial infarction: the quest-stemi study," *Frontiers in Cardiovascular Medicine*, vol. 8, p. 646064, 2021.

[39] M. Pétré, T. Balcaen, W. El Aazmani, G. Pyka, H. Fehervary, N. Famaey, and G. Kerckhofs, "Effect of x-ray contrast-enhancing staining agents on the mechanical properties of blood vessels.," in *Tomography for Scientific Advancement society conference (ToScA)*, 2022.

[40] J. Léonet, J. Vicente, M. de Masi, and V. Deplano, "Contrast-enhanced micro-CT protocol for in-situ mechanical experiments of aortic thrombi," in *48ème Congrès de la société de biomécanique*, pp. S125–S127, 2023.

[41] C. Helfenstein-Didier, D. Taïnoff, J. Viville, J. Adrien, É. Maire, and P. Badel, "Tensile rupture of medial arterial tissue studied by x-ray micro-tomography on stained samples," *Journal of the mechanical behavior of biomedical materials*, vol. 78, pp. 362–368, 2018.

[42] S. Saghamanesh, D. Dumitriu LaGrange, P. Reymond, I. Wanke, K.-O. Lövblad, A. Neels, and R. Zboray, "Non contrast enhanced volumetric histology of blood clots through high resolution propagation-based x-ray microtomography," *Scientific Reports*, vol. 12, no. 1, p. 2778, 2022.

[43] X. Yi, X. Wei, Y. Wang, J. Chen, D. Li, and B. Hu, "Role of real-time elastography in assessing the stage of thrombus.," *International angiology: a journal of the International Union of Angiology*, vol. 36, no. 1, pp. 59–63, 2017.

[44] E. Mfoumou, J. Tripette, M. Blostein, and G. Cloutier, "Time-dependent hardening of blood clots quantitatively measured in vivo with shear-wave ultrasound imaging in a rabbit model of venous thrombosis," *Thrombosis research*, vol. 133, no. 2, pp. 265–271, 2014.

[45] P. Hoang, A. Wallace, M. Sugi, A. Fleck, Y. Pershad, N. Dahiya, H. Albadawi, G. Knuttinen, S. Naidu, and R. Oklu, "Elastography techniques in the evaluation of deep vein thrombosis," *Cardiovascular diagnosis and therapy*, vol. 7, no. Suppl 3, p. S238, 2017.

[46] E. Di Martino, S. Mantero, F. Inzoli, G. Melissano, D. Astore, R. Chiesa, and R. Fumero, "Biomechanics of abdominal aortic aneurysm in the presence of endoluminal thrombus: experimental characterisation and structural static computational analysis," *European Journal of Vascular and Endovascular Surgery*, vol. 15, no. 4, pp. 290–299, 1998.

[47] T. C. Gasser, G. Görgülü, M. Folkesson, and J. Swedenborg, "Failure properties of intraluminal thrombus in abdominal aortic aneurysm under static and pulsating mechanical loads," *Journal of vascular surgery*, vol. 48, no. 1, pp. 179–188, 2008.

[48] G. Martufi, A. Satriano, R. D. Moore, D. A. Vorp, and E. S. Di Martino, "Local quantification of wall thickness and intraluminal thrombus offer insight into the mechanical properties of the aneurysmal aorta," *Annals of biomedical engineering*, vol. 43, pp. 1759–1771, 2015.

[49] Z. Teng, J. Feng, Y. Zhang, Y. Huang, M. P. Sutcliffe, A. J. Brown, Z. Jing, J. H. Gillard, and Q. Lu, "Layer-and direction-specific material properties, extreme extensibility and ultimate material strength of human abdominal aorta and aneurysm: a uniaxial extension study," *Annals of biomedical engineering*, vol. 43, pp. 2745–2759, 2015.

[50] B. J. Doyle, A. Callanan, P. A. Grace, and E. G. Kavanagh, "On the influence of patient-specific material properties in computational simulations: a case study of a large ruptured abdominal aortic aneurysm," *International Journal for Numerical Methods in Biomedical Engineering*, vol. 29, no. 2, pp. 150–164, 2013.

[51] D. Vorp, W. Mandarino, M. Webster, and J. Gorcsan Iii, "Potential influence of intraluminal thrombus on abdominal aortic aneurysm as assessed by a new non-invasive method," *Cardiovascular Surgery*, vol. 4, no. 6, pp. 732–739, 1996.

[52] D. H. Wang, M. S. Makaroun, M. W. Webster, and D. A. Vorp, "Effect of intraluminal thrombus on wall stress in patient-specific models of abdominal aortic aneurysm," *Journal of vascular surgery*, vol. 36, no. 3, pp. 598–604, 2002.

[53] J. P. V. Geest, M. S. Sacks, and D. A. Vorp, "A planar biaxial constitutive relation for the luminal layer of intra-luminal thrombus in abdominal aortic aneurysms," *Journal of biomechanics*, vol. 39, no. 13, pp. 2347–2354, 2006.

[54] K. E. G. O'Leary, SA, P. A. Grace, T. M. McGloughlin, B. J. Doyle, *et al.*, "The biaxial mechanical behaviour of abdominal aortic aneurysm intraluminal thrombus: classification of morphology and the determination of layer and region specific properties," *Journal of biomechanics*, vol. 47, no. 6, pp. 1430–1437, 2014.

[55] J. H. Ashton, J. P. V. Geest, B. R. Simon, and D. G. Haskett, "Compressive mechanical properties of the intraluminal thrombus in abdominal aortic aneurysms and fibrin-based thrombus mimics," *Journal of biomechanics*, vol. 42, no. 3, pp. 197–201, 2009.

[56] E. A. van Dam, S. D. Dams, G. W. Peters, M. Rutten, G. W. H. Schurink, J. Buth, and F. N. van de Vosse, "Determination of linear viscoelastic behavior of abdominal aortic aneurysm thrombus," *Biorheology*, vol. 43, no. 6, pp. 695–707, 2006.

[57] J. Hinnen, D. Rixen, O. Koning, J. van Bockel, and J. Hamming, "Development of fibrinous thrombus analogue for in-vitro abdominal aortic aneurysm studies," *Journal of biomechanics*, vol. 40, no. 2, pp. 289–295, 2007.

[58] E. A. van Dam, S. D. Dams, G. W. Peters, M. C. Rutten, G. W. H. Schurink, J. Buth, and F. N. van de Vosse, "Non-linear viscoelastic behavior of abdominal aortic aneurysm thrombus," *Biomechanics and modeling in mechanobiology*, vol. 7, pp. 127–137, 2008.

[59] F. Ghezelbash, S. Liu, A. Shirazi-Adl, and J. Li, "Blood clot behaves as a poro-visco-elastic material," *Journal of the Mechanical Behavior of Biomedical Materials*, vol. 128, p. 105101, 2022.

[60] M. A. Biot, "General theory of three-dimensional consolidation," *Journal of applied physics*, vol. 12, no. 2, pp. 155–164, 1941.

[61] M. Bukač and S. C. Shadden, "Quantifying the effects of intraluminal thrombi and their poroelastic properties on abdominal aortic aneurysms," *Archive of Applied Mechanics*, pp. 1–12, 2021.

[62] M. Toungara and C. Geindreau, "Influence of a poro-mechanical modeling of the intra-luminal thrombus and the anisotropy of the arterial wall on the prediction of the abdominal aortic aneurysm rupture," *Cardiovascular Engineering and Technology*, vol. 4, pp. 192–208, 2013.

[63] V. Deplano, M. Boufi, O. Boiron, C. Guivier-Curien, Y. Alimi, and E. Bertrand, "Biaxial tensile tests of the porcine ascending aorta," *Journal of biomechanics*, vol. 49, no. 10, pp. 2031–2037, 2016.

[64] O. Chaudhuri, J. Cooper-White, P. A. Janmey, D. J. Mooney, and V. B. Shenoy, "Effects of extracellular matrix viscoelasticity on cellular behaviour," *Nature*, vol. 584, no. 7822, pp. 535–546, 2020.